Ultrahigh Permeability at High Frequencies via A Magnetic-Heterogeneous Nanocrystallization Mechanism in an Iron-Based Amorphous Alloy

Jing Zhou, Xuesong Li, Xibei Hou, Haibo Ke, Xingdu Fan, Junhua Luan, Hailong Peng, Qiaoshi Zeng, Hongbo Lou, Jianguo Wang, Chain Tsuan Liu, Baolong Shen, Baoan Sun,* Weihua Wang, and Haiyang Bai*

The prevalence of wide-bandgap (WBG) semiconductors allows modern electronic devices to operate at much higher frequencies. However, development of soft magnetic materials with high-frequency properties matching the WBG-based devices remains challenging. Here, a promising nanocrystalline–amorphous composite alloy with a normal composition $Fe_{75.5}Co_{0.5}Mo_{0.5}Cu_1Nb_{1.5}Si_{13}B_8$ in atomic percent is reported, which is producible under industrial conditions, and which shows an exceptionally high permeability at high frequencies up to 36 000 at 100 kHz, an increase of 44% compared with commercial FeSiBCuNb nanocrystalline alloy (25 000 ± 2000 at 100 kHz), outperforming all existing nanocrystalline alloy systems and commercial soft magnetic materials. The alloy is obtained by a unique magnetic-heterogeneous nanocrystallization mechanism in an iron-based amorphous alloy, which is different from the traditional strategy of nanocrystallization by doping nonmagnetic elements (e.g., Cu and Nb). The induced magnetic inhomogeneity by adding Co atoms locally promotes the formation of highly ordered structures acting as the nuclei of nanocrystals, and Mo atoms agglomerate around the interfaces of the nanocrystals, inhibiting nanocrystal growth, resulting in an ultrafine nanocrystalline–amorphous dual-phase structure in the alloy. The exceptional soft magnetic properties are shown to be closely related to the low magnetic anisotropy and the unique spin rotation mechanism under alternating magnetic fields.

1. Introduction

The prevalent application of the wide-bandgap (WBG) semiconductors allows modern electronics to operate at much higher frequencies, leading to the whole industry developing towards high frequency, high power, miniaturization, and energy saving.[1,2] For example, WBG semiconductors are usually used in conjunction with soft magnetic devices in current converters, which play the role of energy storage and transmission.[3–5] However, the soft magnetic materials available today are unable to reach their full potential to meet the needs of WBG-based devices at high frequencies. With the increase of frequency, permeability becomes one of the most important parameters to determine performance of electronic devices. The permeability characterizes the response ability of soft magnetic materials to external magnetic fields,[6] and thus determines magnetization impedance, and ultimately determines the sensitivity and electromagnetic compatibility of electronic devices.[7] Therefore, the high-frequency permeability is particularly required for electronic devices

J. Zhou, X. Li, X. Hou, H. Ke, B. Sun, W. Wang, H. Bai
Songshan Lake Materials Laboratory
Dongguan 523808, China
E-mail: sunba@iphy.ac.cn; hybai@iphy.ac.cn

J. Zhou, B. Sun, W. Wang, H. Bai
Institute of Physics
Chinese Academy of Sciences
Beijing 100190, China

J. Zhou, J. Wang, W. Wang
School of Mechanical Engineering
Dongguan University of Technology
Dongguan 523808, China

X. Li, W. Wang
School of Energy Power and Mechanical Engineering
North China Electric Power University
Beijing 102206, China

X. Fan, B. Shen
School of Materials Science and Engineering
Southeast University
Nanjing 211189, China

J. Luan, C. T. Liu
Department of Materials Science Engineering
College of Science and Engineering
City University of Hong Kong
Hong Kong 999077, China

**ADVANCED
SCIENCE NEWS**

www.advancedsciencenews.com

**ADVANCED
MATERIALS**

www.advmat.de

operating at high frequencies. However, the permeability of most soft magnetic materials decays rapidly with increasing frequency, which has become a major obstacle in matching WBG-based device applications.

Since the discovery of the soft magnetic pure iron more than a century ago, the improvement of high-frequency permeability of soft magnetic materials has been the long-standing goal of researchers, and has become increasing urgent over the past decade. To date, a variety of materials have been reported, including pure iron,[1] silicon steels,[8] ferrites,[9] and amorphous/nanocrystalline alloys.[10,11] Among them, Fe-based nanocrystalline alloys, mostly obtained by annealing their amorphous precursors to induce nanocrystals in amorphous matrix, are regarded as the most promising next-generation of soft magnetic materials because of their excellent comprehensive soft magnetic properties.[10] However, the high-frequency effective permeability (μ_e) of these alloys is still limited. So far, the highest value of the μ_e reported in soft magnetic alloys is generally no more than 25 000 at 100 kHz, except for those ultrathin nanocrystalline ribbons. In the past few decades, extensive efforts have been devoted, and many strategies have been proposed to improve soft magnetic properties of nanocrystalline alloys, e.g., microalloying techniques[6,12–14] and producing thinner amorphous ribbons.[15,16] In development of better nanocrystalline alloys, the challenge lies in achieving high permeability at high frequency while maintaining other magnetic properties such as the high saturation magnetic flux density (B_s) and the low core loss (P_{cv}). In addition, the recently developed nanocrystalline alloys often exhibit both of deterioration of soft-magnetic properties and poor manufacturability under industrial conditions, which are not expected in practical applications.

As we know, the size and morphology of nanocrystals play key roles in soft magnetic properties of nanocrystalline alloys, which depend mainly on nucleation and growth mechanisms of nanocrystals during annealing. The addition of nonmagnetic Cu and Nb elements to FeSiB amorphous alloys is the most common and classical method to optimize the structure of nanocrystals.[17–19] The famous $Fe_{73.5}Si_{13.5}B_9Cu_1Nb_3$ alloy[10] (known as FINEMET, first reported in 1988) was obtained by this method and exhibits stable and fine nanocrystals, resulting in a great leap forward in the soft magnetic properties compared with traditional magnetic amorphous alloys. Hitherto, commercial FINEMET nanocrystalline alloy with optimal thermal treatment has the highest permeability at high frequencies among all soft magnetic materials. Despite extensive research, there has been no breakthrough in the development of better soft magnetic materials, except for obtaining ultrathin ribbon samples

by optimizing of manufacturing process.[15,16] Based on the conventional nanocrystallization strategy, there is very little room for further refinement of nanocrystals. Therefore, innovation of the nanocrystallization mechanism and further refinement of nanocrystalline structure are the key to break through the limits of soft magnetic properties of Fe-based nanocrystalline alloys.

Here, we report a unique magnetic-heterogeneous nanocrystallization mechanism where Fe–Co magnetic atomic clusters act as the nuclei of nanocrystals under the external magnetic field, and Mo atoms agglomerate around the interfaces of nanocrystals, resulting in the Nb, Mo, and Si multielement gradient enrichment structure, thereby inhibiting the nanocrystal growth, which is totally different from the conventional nanocrystallization mechanism based on nonmagnetic Cu and Nb. The unique nanocrystallization mechanism leads to an ultrafine nanocrystalline structure. This alloy consequently shows an ultrahigh permeability at high frequencies, along with considerably low P_{cv} and high B_s. The combination of these features is attractive and of basic significance for high-frequency applications. The physical mechanisms underlying these superior high-frequency properties are discussed from the perspective of the magnetic anisotropy, unique magnetic-domain structures, and their motions in the Fe-based alloy.

2. Results and Discussion

2.1. Nanocrystalline–Amorphous Dual-Phase Structure

A base alloy of $Fe_{76.5}Cu_1Nb_{1.5}Si_{13}B_8$ (denoted as FS, at atomic precents) was selected for microalloying.[13] Trace amounts of Co and Mo were simultaneously added into the base alloy to partially replace Fe, yielding the composition of $Fe_{75.5}Co_{0.5}Mo_{0.5}Cu_1Nb_{1.5}Si_{13}B_8$ (denoted as FCMS). For comparison, $Fe_{76}Co_{0.5}Cu_1Nb_{1.5}Si_{13}B_8$ (denoted as FCS) and $Fe_{76}Mo_{0.5}Cu_1Nb_{1.5}Si_{13}B_8$ (denoted as FMS) were also prepared by microalloying Co or Mo into the base alloy, respectively. The as-quenched ribbon samples of all compositions show a broad halo with no sharp diffraction peaks on the X-ray diffraction (XRD) curves (Figure S1a, Supporting Information), indicating fully amorphous nature of these samples. The amorphous structure of ribbons was further verified by the typical maze-like patterns in the images of transmission electron microscope (TEM) (Figure S1b, Supporting Information). After 20 min of transverse magnetic field annealing, TEM image shows that FS alloy exhibits an amorphous–nanocrystalline dual-phase structure (**Figure 1**a). From the magnified images (Figure 1b,c), one can see that the grain shape is irregular, and the average grain size is 20.4 nm (Figure 1d). In contrast, FCMS has quite different microstructure compared to FS. FCMS possesses an ultrafine nanocrystalline–amorphous dual-phase structure where nanocrystalline grains are uniformly distributed in the amorphous matrix (Figure 1e). High-resolution TEM images of a local area of FCMS (Figure 1f,g) show that the precipitated nanocrystals are equiaxed grains with good roundness, in sharp contrast to those in FS. Selected-area electron diffraction (SAED) patterns confirm that these nanocrystals are α-Fe (Co) phases (inset of Figure 1e) with the distance between (110) planes of 2.0115 Å (Figure 1g). The average size of nanocrystals is as small as 11.8 nm (Figure 1h), which is only half of that in FS. The volume

H. Peng
School of Materials Science and Engineering
Central South University
932 South Lushan Rd, Changsha 410083, China

Q. Zeng, H. Lou
Center for High Pressure Science and Technology Advanced Research
Pudong, Shanghai 201203, China

B. Sun, W. Wang, H. Bai
Center of Materials Science and Optoelectronics Engineering
University of Chinese Academy of Sciences
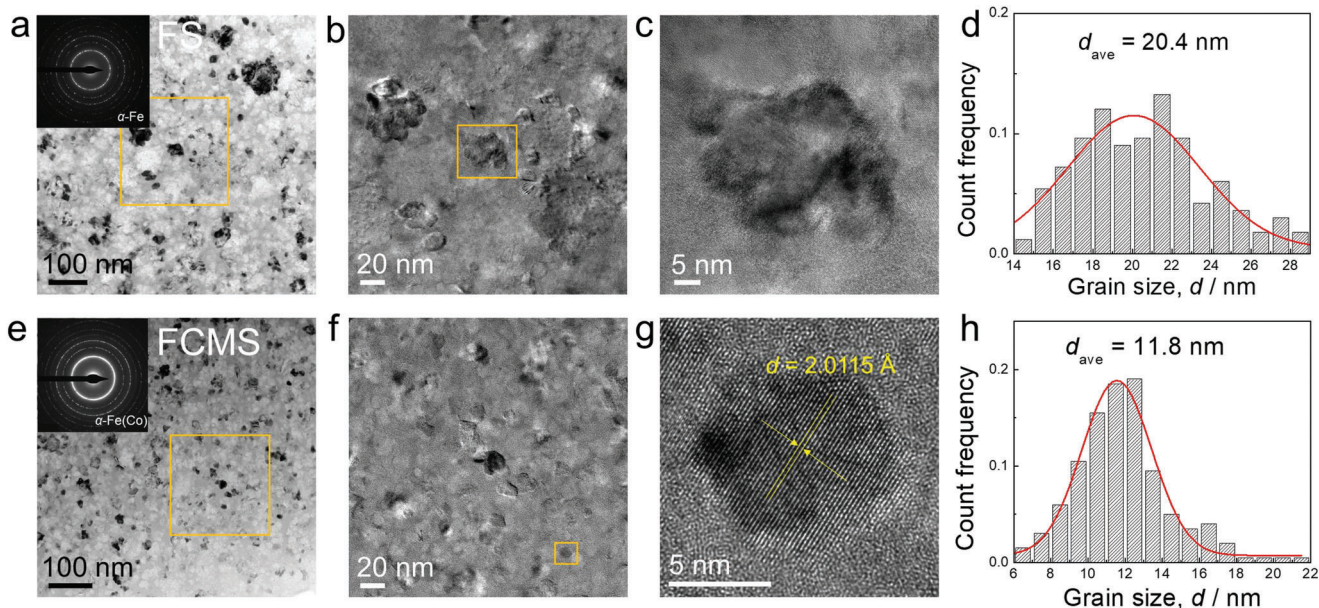Beijing 100049, China

**ADVANCED
SCIENCE NEWS**

www.advancedsciencenews.com

**ADVANCED
MATERIALS**

www.advmat.de

Figure 1. Microstructures of FS and FCMS nanocrystalline alloy ribbons. a,e) Bright-field TEM images and SAED patterns of optimal annealed FS (a) and FCMS (e). b,f) Enlarged images of the orange square areas in (a) and (e), respectively. c,g) Enlarged images of the orange square areas in (b) and (f), respectively. d,h) Grain size distributions of optimal annealed FS (d) and FCMS (h).

fraction of α-Fe (Si) nanograins (V_{cry}) was estimated using the method by analyzing the bright-field TEM image (see the Experimental Section). The evaluated crystallization volume fraction of FCMS is estimated as 71.2%, which is higher than that of FS with a crystallization volume fraction of 66.4%. The grain boundary density of FCMS (0.36 nm^{-1}) is also higher than that of FS (0.195 nm^{-1}), in consistent with the results of crystallization volume fraction. The high-angle annular dark-field (HAADF)-STEM image clearly confirmed the ultrafine nanocrystalline–amorphous dual-phase structure of FCMS (Figure S2a, Supporting Information). In addition, Figure S2b (Supporting Information) shows the corresponding energy-dispersive X-ray spectroscopy (EDS) linear scanning of Fe, Co, Nb, Mo, and Cu elements across the grain of FCMS (marked by the white dash line in Figure S2a (Supporting Information). Noted that it is difficult to observe Cu clusters directly in TEM image of the both alloys, since the concentration of Cu is quite small, and its atomic scattering factor is close to that of Fe.[20] Although the TEM line scanning represents the distribution information of elements in a certain plane and is difficult to accurately locate the position of Cu clusters, the preliminary characterization shows that Fe and Co elements are enriched in the grain interior, while Nb and Mo elements are concentrated at the grain boundary.

It is worth noting that there is possibility that the finer size of the nanoprecipitates may also arise from an increase in the content of Nb or (Nb + Mo). To check the possibility, we prepared a Fe$_{76}$Cu$_1$Nb$_2$Si$_{13}$B$_8$ (denoted as FS′) ribbon sample (increasing the Nb content of FS from 1.5 to 2%) and measured its microstructure (shown in Figure S3, Supporting Information). It can be seen that most of the particles of FS′ nanocrystalline alloy show irregular shapes. The average grain size of nanoprecipitates is around 18.5 nm, which is larger than that in FCMS (Figure 1f). Therefore, increasing the content of Nb indeed can reduce the

grain size as compared to the FS alloy, however, only by adding Co and Mo simultaneously can result in extremely fine nanocrystals. This suggests that simultaneous addition of Co and Mo has unexpected effects on both the grain nucleation and growth process, thus plays a key role in the formation of extremely fine nanocrystals.

2.2. Nanocrystallization Mechanism

In order to interpret the formation mechanism of the ultrafine nanocrystalline structure in FCMS, high-resolution atomic probe tomography (APT) was employed to analyze the element distribution in and around nanocrystals with a comparison with FS. It is noteworthy that the iso-surface coincides well with the grain interface when the content of B element is about 5% atomic percent. Therefore, the interface between nanocrystals and matrix was marked with 5% content of B element in all element mappings (**Figure 2**a, Figures S4 and S6, Supporting Information). In addition, the iso-surfaces highlighting method leads to the observation of blue particles in APT results (Figures S4 and S6, Supporting Information), which are not the B-rich compounds, but the boundaries of grains viewed from a two-dimensional. For the FS alloy (Figure S4a, Supporting Information), it can be seen that the Cu atoms gathered into clusters around nanograins, while Nb element mainly segregates in the amorphous matrix surrounding the α-Fe (Si) grains. The depth profiles shown in Figure S4b (Supporting Information) indicate clearly that the Nb content is depleted within the grain and rapidly increases across the crystalline–amorphous interfaces. The element distributions in FS are consistent with those of traditional nanocrystalline alloys reported previously.[21] The nanocrystallization mechanism is well recognized: Cu atoms gathered into clusters serving as
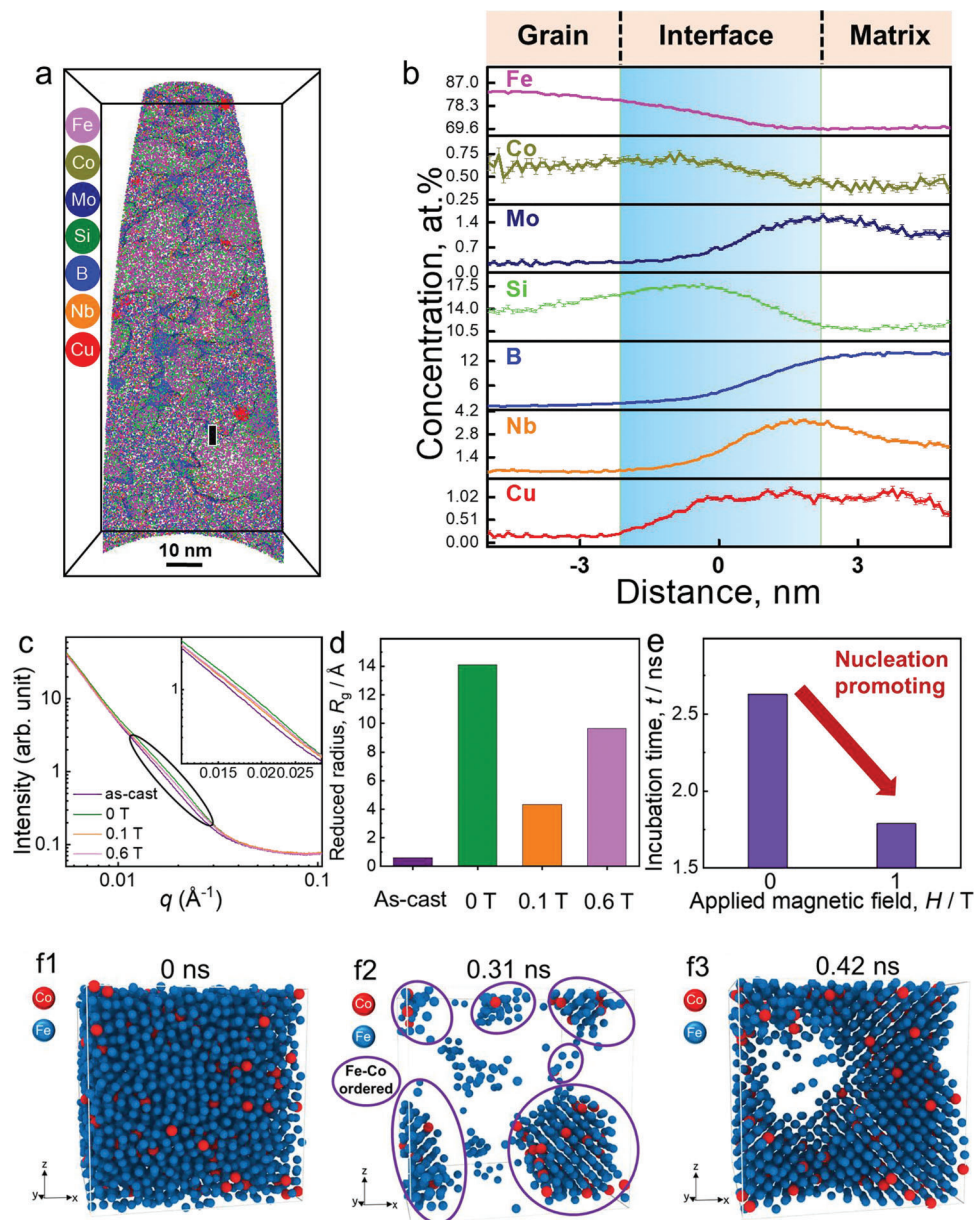
Figure 2. Experimental observation and simulation analysis for the formation of ultrafine nanocrystal. a) Elemental maps of the FCMS. b) Concentration depth profiles from the selected cylindrical region of FCMS showing in (a). c) Representative SAXS data of as-cast and annealed FCMS samples under magnetic field of 0 T, 0.1 T, and 0.6 T, respectively, the inset is an enlarged view of the ellipse region in (c). The as-cast sample is homogeneous according to its monotonically decayed data, whereas a hump at ≈ 0.02 Å^{-1} is observed after annealing treatment, indicating density fluctuation emerges. d) The comparison of R_g value of as-cast and annealed samples under magnetic field of 0 T, 0.1 T, and 0.6 T, respectively. e) Incubation time of FCMS under magnetic field assisted heat treatment at different applied magnetic field (0 T and 1 T). f) The molecular dynamics simulation of the atomic motion of $Fe_{95}Co_5$ alloy at different incubation periods of 0 ns (f1), 0.31 ns (f2), and 0.42 ns (f3) during the crystallization process under an external magnetic field of 1 T. (f1) shows all the atoms, and (f2) and (f3) show only the atoms of the (approaching) crystal phase. Fe atoms are colored in blue and Co atoms are colored in red.

inhomogeneous nucleation sites of nanograins, and Nb atoms are enriched in the amorphous matrix to inhibit the interface growth of crystals (Figure S5a, Supporting Information). While for the FCMS alloy, the element distributions become more complicated after minor addition of Co and Mo. The element mapping (Figure S6, Supporting Information) and depth profiles (Figure 2a) show that Co is enriched in α-Fe nanocrystals, and

reduced greatly in the amorphous matrix, similar to the distribution of Fe. It can be seen that the content of Co element in nanocrystals is about 0.7 at% by analyzing the distribution, which is much higher than that of 0.3 at% in amorphous matrix. Since Co has similar atomic size and properties with Fe, Co atoms can dissolve into the crystal lattice of α-Fe to form substitutional solid solution. Meanwhile, Mo is segregated at the intersection of the

**ADVANCED
SCIENCE NEWS**

www.advancedsciencenews.com

**ADVANCED
MATERIALS**

www.advmat.de

interface and the amorphous matrix, similar with the distribution of Nb. The element distributions of Co and Mo presented by APT (Figure 2b) are also consistent with the linear element analysis across a nanocrystal by high-resolution TEM (Figure S2b, Supporting Information). The depth profiles also show the extra-enrichment of Si in the interface regions between the grains and amorphous matrix, indicating the initial formation of a transient Si-rich shell. The Nb, Mo, and Si multielement gradient enrichment structure is expected to stabilize the matrix and inhibit the α-Fe grain growth.[12]

Based on the element distributions, we deduce a unique nanocrystallization mechanism for FCMS, as illustrated in Figure S5b (Supporting Information). The Co addition introduces Co–Co and Fe–Co pairs, exhibiting different exchange integrals as compared to Fe–Fe pairs, resulting in significant fluctuations of exchange energies and local anisotropy in the as-cast ribbons. Once the external magnetic field is applied, such energy and magnetic heterogeneity will be further amplified, resulting in significant fluctuations of the local stress field around Co atoms, since the magnetic moments of the Fe and Co atoms are 2.2 and 1.7 μ_B, respectively. The structural rearrangement occurs preferentially at these locations with high internal stress, promoting the development of highly ordered structures (HOS).[22] As the cores of uniform nucleation, this HOS preferentially grow into the body-centered-cubic crystal structure. In addition, Mo has the large mixing enthalpy and the large mismatch of atomic radii with other elements,[23] leading to complex diffusion and agglomeration of shells at grain boundaries to promote grain refinement. As compared to the FS, although the number of elements in the nanocrystal is increased in FCMS, the content of Co is in fact very low, which is about 0.7 at% according to the APT results. Such a low content of Co will have little effect on increasing the configurational entropy of nanocrystals. Therefore, the smaller size of nanocrystals in FCMS cannot be attributed to the effects of multiple elements (high-entropy effect) contained in nanocrystals. However, the segregation of Mo around the grain boundaries, which co-acts with Nb, can lead to a higher level of atomic confusion and crowding at the interfaces, which increase the energy barrier of the interfaces and further inhibit grain growth. Therefore, the doping of Co and Mo elements results in a unique nanocrystallization process, which is different from the traditional nanocrystallization strategy used in Fe-based amorphous alloys over the past decades.[21] The present mechanisms caused by Co and Mo dominate the nucleation and growth of nanocrystals during annealing, resulting in the formation of ultrafine nanocrystalline–amorphous dual-phase structure.

Since the APT data can only reflect the state of the alloy after crystallization, which is not enough to fully elaborate the crystallization process, the differential scanning calorimetry (DSC) test, synchrotron small-angle X-ray scattering (SAXS) measurements, and molecular dynamics simulations were also carried out to further verify the existence of the unique nanocrystallization process. Figure S7a (Supporting Information) shows the DSC curves of the FCMS pre-annealing at 653 K (about $T_{x1} - 100$ K) for 30 min under the transverse magnetic fields of 0, 0.05, 0.1, and 0.6 T, respectively. It can be seen that T_{x1} obviously shows a trend of first decreasing and then increasing with the increase of the external magnetic field, and reaching the minimum value when

the external magnetic field is 0.1 T. The results suggest that the application of appropriate external magnetic field promotes indeed the nanocrystallization process of FCMS. Subsequently, the isothermal experiments were performed by DSC at the temperature of 748 K (about $T_{x1} - 5$ K), as shown in Figure S7b (Supporting Information). Assuming that the volume transition rate of the crystallization is proportional to the measured heat flow, we can obtain the crystallized fraction (x) values of FCMS versus isothermal time (t), as shown in Figure S7c (Supporting Information). As compared with the sample without external magnetic field (0 T), we can see clearly that the sample under the external magnetic field (0.1 T) exhibits the highest crystallization rates during the isothermal process. In addition, Figure 2c shows the SAXS data from 0.0055 to 0.1 Å^{-1} of as-cast sample, and annealed samples under the magnetic field of 0, 0.1, and 0.6 T, respectively. It can be seen that a hump caused by density fluctuation emerges at ≈0.02 Å^{-1} after annealing treatment, indicating that the short-range fluctuations with different states occurred in the samples. Notably, the amplitude of the hump decreases to its lowest level in the presence of external magnetic fields of 0.1 T. This also suggests that the suitable applied magnetic field, can promote the formation of smaller crystalline nuclei in the glassy matrix. The crystalline nuclei radius, R_g, obtained by Guinier-porod fitting on SAXS data[24] is widely used to determine the size and dimensionality of scattering objects. Figure 2d shows the comparison of R_g of the as-cast and annealed samples under different magnetic fields. Again, the as-cast sample shows a relatively homogeneous structures with R_g smaller than the length of atomic bond, indicating that there are no crystal nuclei in the as-cast sample. In contrast, the pre-annealing sample in the absence of magnetic field has the largest R_g reaching 14 Å. By applying proper magnetic field of 0.1 T during annealing, R_g decreases to a minimum value of 4.3 Å. We speculate that, when the external magnetic field is applied during nanocrystallization process, the magnetization state of the ferromagnetic matrix will change and generate internal stress, in order to keep the total energy of the ferromagnetic matrix at a minimum state, which is balanced by the coupling energy of spin-orbit and the elastic energy of the material. Due to the difference of magnetic moment rotation angles of Fe and Co in magnetostrictive effect under different external magnetic fields, stress concentrations and energy fluctuations will occur at sites enriching Co atoms. When the energy fluctuation effect reaches maximum, the corresponding external magnetic field will induce the largest amount of nucleation sites. While with the external magnetic field intensity increasing further, the magnetic moment rotation process is gradually completed, and the energy fluctuation effect near Fe and Co atoms is weakened. Therefore, the R_g decreases first and then increases with applied magnetic field. The SAXS result confirms that suitable magnetic field annealing (0.1 T) will promote the formation of smaller crystalline nuclei in the FCMS samples, which is a distinct phenomenon of medium-range ordering that further involved in the nucleation of tiny nanocrystals in FCMS.

In order to elucidate the contribution of Co in promoting nucleation, we also performed molecular dynamics simulation on the nucleation process of a typical binary $Fe_{95}Co_5$ amorphous alloy under the condition of applied magnetic fields. Details of the simulation experiment are shown in the Experimental

Section. Typical results under the magnetic field of 1 T are shown as Figure 2f1–3. From the figure, one can see that the distribution of Fe and Co atoms and their evolution process during the crystallization. At 0 ns, the Fe and Co atoms are completely disorganized. When the relaxation time reaches to 0.31 ns, Fe and Co atoms begin to form some ordered clusters which are at a transition state between nanocrystals and amorphous state. These transition clusters are mainly rearranged with Fe–Co atom pairs, which act as the nucleation core (marked by purple oval) of nanocrystals. As the relaxation time continues (0.42 ns), these ordered clusters gradually grow into a α-Fe (Co) nanocrystal. The average incubation time of crystallization also decreases with the increase of applied magnetic field (Figure 2e), and reaches a minimum value of 1.8 ns with the applied magnetic field of 1 T, which further confirms that the application of external field can obviously promote the nucleation of FCMS.

2.3. Magnetic Properties and Manufacturability

We further performed systematic investigation on the thermal and magnetic properties of FCMS, FMS, FCS, FS, and FS′ alloys. The DSC curves show that all alloys exhibit two sharp crystallization peaks with relatively high onset T_{x1} and a large ΔT_x ($T_{x2} - T_{x1}$) values of more than 150 K (Figure S8a, Supporting Information). The T_{x1} and T_{x2} correspond to the precipitation of soft magnetic α-Fe phase[17,25] and hard magnetic Fe_2B phase,[26] respectively. Therefore, the larger ΔT_x suggests a larger processing window to modulate nanocrystalline structures during annealing. Interestingly, an obvious glass-transition endothermic step was observed in FCMS (Figure S8b, Supporting Information), which is rare for Fe-based amorphous alloys with high content of Fe,[27] indicating that FCMS exhibits a high amorphous forming ability and good potential for industrial production. The as-quenched ribbons were annealed at 853 K under a magnetic field for different times to yield nanocrystalline alloys. As shown in Figure S9a (Supporting Information), all nanocrystalline samples exhibit a hysteresis loop typical of soft magnetic alloys. The values of B_s of these alloys are comparable, ranging between 1.4 and 1.42 T, dependent on the content of Fe. Among them, FCMS exhibits the highest value of B_s up to 1.42 T, indicating that minor doping of Co is beneficial for improving the B_s. The relationship between the annealing time and coercivity (H_c) for FS′, FS, FCS, FMS, and FCMS ribbons is also shown in Figure S9b (Supporting Information). One can see that increasing the content of Nb to 2.0 at.% does reduce effectively the H_c of the sample as compared to that of FS and FCS. The H_c of FS′ is comparable to that of FMS, but is still slightly higher than that of FCMS. Among them, FCMS shows the lowest value of 0.9 A m^{-1} at the annealing time of 20 min. The H_c of FCMS is decreased by about 70% as compared with that at the annealing time of 10 min, and remains at a low level in the time range of 15 to 30 min. The low annealing sensitivity of H_c is also desired in industrial applications.

With a good amorphous forming ability, wide amorphous ribbons of the FCMS ($\approx$63 mm in width) were successfully prepared under industrial conditions. Then, the ribbons were cut and wound into magnetic cores and annealed into nanocrystalline alloys (Figure S10, Supporting Information). The μ_e and P_{cv} of FCMS magnetic cores were measured at different frequencies and then compared with the commercial FeSiBCuNb nanocrystalline alloy (nominal composition of $Fe_{73.5}Si_{13.5}B_9Cu_1Nb_3$),[10] which exhibits hitherto the highest μ_e at high frequencies among all soft magnetic materials. It should be noted that in order to ensure the comparability of data, FCMS and commercial FeSiB-CuNb nanocrystalline alloy ribbons with the same thickness of 18 μm were selected for comparison. Figure S11 (Supporting Information) shows frequency dependence of the μ_e for the FCMS and commercial FeSiBCuNb nanocrystalline alloy from 1 kHz to 1 MHz. It can be seen that at low frequencies (<30 kHz), the μ_e of FCMS is slightly lower than that of FeSiBCuNb nanocrystalline alloy, but it still remains above 80 000. At high frequencies (>30 kHz), as shown in **Figure 3**a,b, the μ_e of FCMS is dramatically increased as compared with commercial FeSiBCuNb nanocrystalline alloy, and the increment becomes more significant as the frequency goes up. The μ_e increases by 20% at 50 kHz, 44% at 100 kHz, 53% at 500 kHz, and reaches to 65% at 1 MHz. The average value of μ_e of FCMS cores is 35 000 $\pm$ 1000 at 100 kHz with the highest value reaching 36 000 (Figure 3a). The fluctuation of the measured μ_e among FCMS cores can be attributed to the small fluctuation on surface roughness, thickness, and alloy compositions in industrial ribbons for making the cores.

Figure 3c,d also displays the P_{cv} at the frequencies from 500 kHz to 1 MHz (falling into the frequency range of the WBG-based devices) under a magnetic field of 50 mT and at the applied magnetic field from 0.05 to 0.8 T under a frequency of 100 kHz, respectively. One can see that the P_{cv} of FCMS is slightly lower than that of commercial FeSiBCuNb nanocrystalline alloy at all high frequencies and applied magnetic fields. Here, it is worth mentioning that, by modulating the microstructure of nanocrystals through microalloying, a synergy between high μ_e and low P_{cv} is achieved in FCMS. Furthermore, the FCMS shows not only the lower values of P_{cv} at each magnetic field, but also a higher limit of magnetic flux density (B_m) when magnetized in alternating current state, as shown in Figure 3e. It can be seen that FCMS maintains larger values of B_m from 50 Hz to 1 MHz. The high B_m of FCMS is closely related to its high B_s (1.42 T) at direct current state, which is higher than that of commercial FeSiBCuNb nanocrystalline alloy at 1.26 T (Figure 3f). The characteristic of maintaining high magnetization at high frequencies for FCMS is attractive for high power and/or miniaturization of high-frequency electromagnetic devices.

The reported data on magnetic permeability of soft magnetic materials at high frequencies are mainly concentrated around 100 kHz. The μ_e and B_s values of FCMS, other typical amorphous/nanocrystalline alloys[10,12,13] and previously reported soft magnetic materials[28–45] are summarized and compared at 100 kHz (**Figure 4**a). It can be seen that the optimal μ_e and B_s of FCMS core reach 36 000@100 kHz and 1.42 T, respectively, realizing a combination of the highest μ_e and relatively higher B_s among all soft magnetic materials. In addition, Figure 4b shows the relationship between B_s and P_{cv} at 0.2 T and 100 kHz of typical soft magnetic materials. It can be seen that the P_{cv} of the FCMS is 120 kW m^{-3} at 0.2 T and 100 kHz, which is also much lower than that of other soft magnetic materials reported in the literature.[46]

We have also summarized the changes in manufacturing cost with effective permeability at the frequency of 100 kHz of several typical Fe-based nanocrystalline alloys (Figure 4c). Here, we
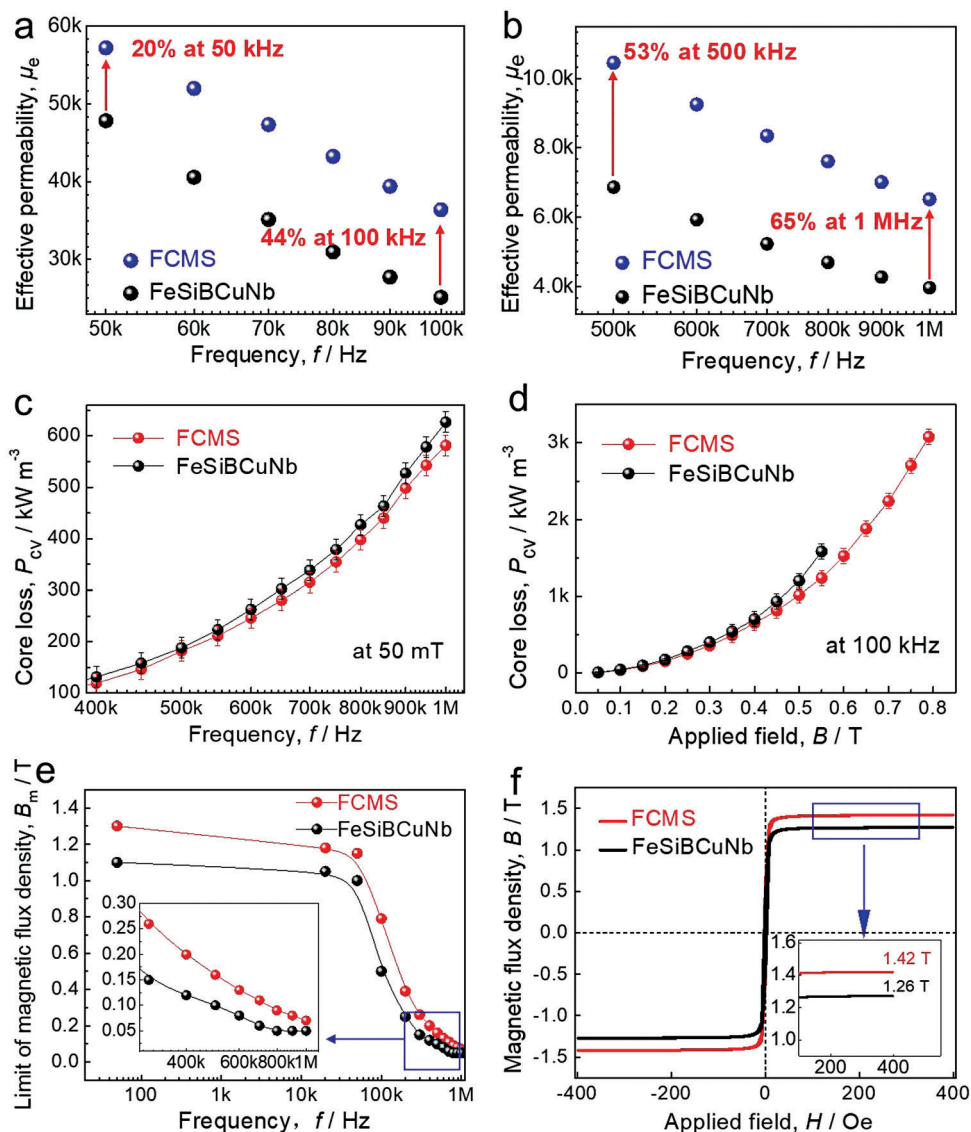
**ADVANCED
SCIENCE NEWS**

www.advancedsciencenews.com

**ADVANCED
MATERIALS**

www.advmat.de

Figure 3. Magnetic properties of the wound and annealed core samples of FCMS and commercial FeSiBCuNb nanocrystalline alloy. Frequency dependence of the effective permeability for the FCMS and commercial FeSiBCuNb nanocrystalline alloy from 50 to 100 kHz (a) and 500 kHz to 1 MHz (b). c) Dependence of P_{cv} at the frequency from 500 kHz to 1 MHz under the magnetic field of 50 mT of FCMS and commercial FeSiBCuNb nanocrystalline alloy. d) The P_{cv} as a function of applied magnetic field at the frequency of 100 kHz of FCMS and commercial FeSiBCuNb nanocrystalline alloy. e) Frequency dependence of the limit magnetic flux density for the FCMS and commercial FeSiBCuNb nanocrystalline alloys from 50 Hz to 1 MHz, the inset is an enlarged view of rectangular region in (e). f) B–H curves of proper annealed FCMS and commercial FeSiBCuNb nanocrystalline alloys with partially enlarged drawing inserted.

evaluate the manufacturing cost of FCMS and commercial Fe-CuNbSiB (FINEMET), Fe-(Zr,Nb,Hf)-B (HITPERM), and FeCo-(Zr,Nb)-B (NANOPERM) nanocrystalline alloys by comparing their market prices of raw materials. Similar comparison method is also used by other researchers.[12,17] In the figure, the NANOPERM and HITPERM alloys have not been industrialized owing to their poor formability and economic limitations, while the FINEMET alloy has been successfully commercialized because of its low manufacturing cost and excellent comprehensive properties. Compared with FINEMET, FCMS has better comprehensive soft magnetic properties and lower cost due to the reduction of the content of Nb and other noble metals. In addition, FCMS also

has a comparable manufacturability compared with FINEMET, since wide FCMS ribbons with a width of 63 mm can be successfully fabricated under industrial conditions with better surface quality and flexural ductility (inset of Figure 4c).

To further highlight the high μ_e of the FCMS at high frequencies, we summarized the development of high-frequency μ_e in soft magnetic materials over the past century (Figure 4d). It can be clearly seen that the μ_e at 100 kHz has been continuously improved with the development of soft magnetic materials since the discovery of pure iron in 1885.[1] However, the μ_e at 100 kHz had been less than 15 000 until the FINEMET nanocrystalline alloys with a permeability of 25 000 ± 2000 came out in 1988.[10] In the
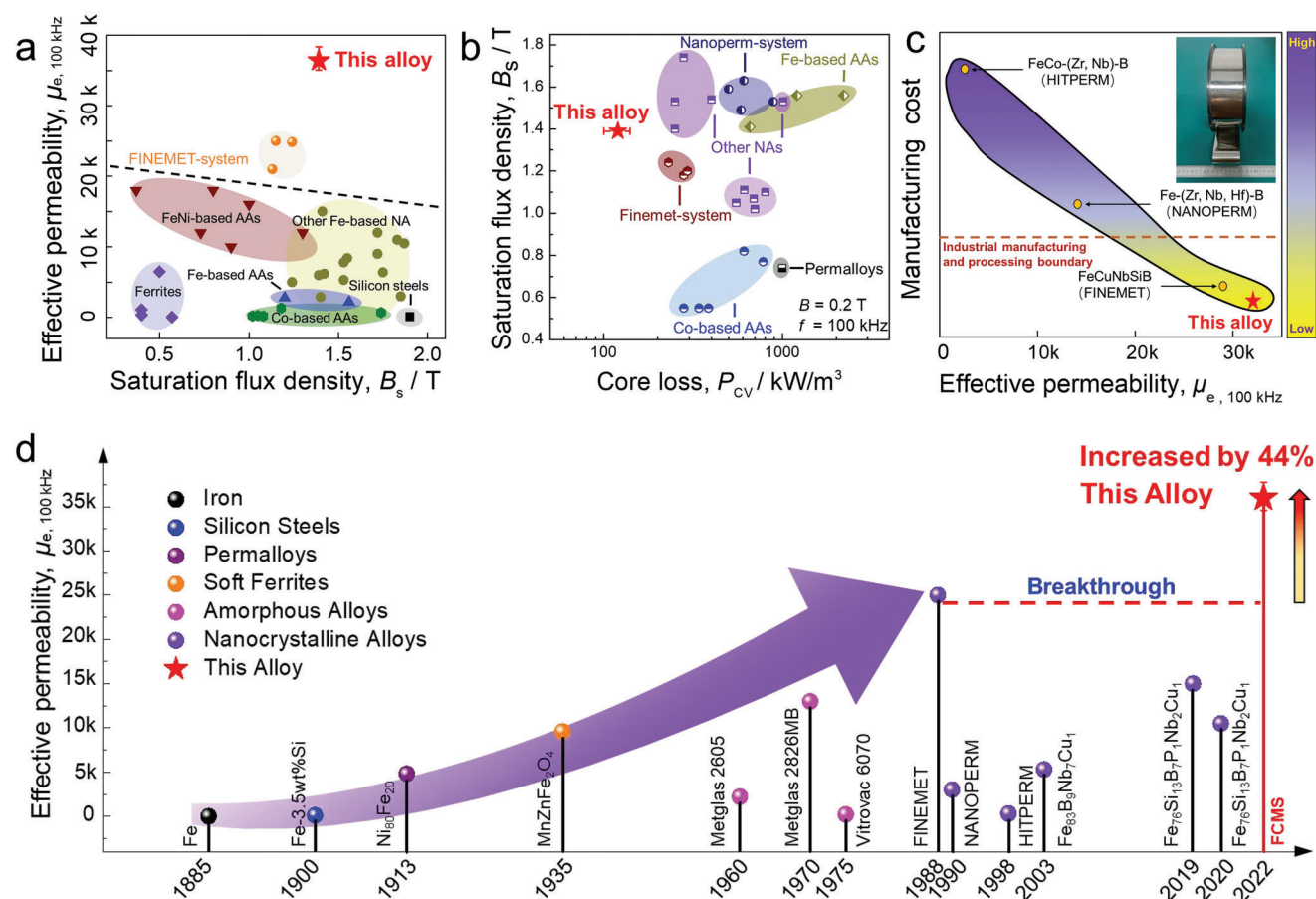
**ADVANCED
SCIENCE NEWS**

www.advancedsciencenews.com

**ADVANCED
MATERIALS**

www.advmat.de

Figure 4. Summary of the soft magnetic properties (e.g., μ_e, B_s, and P_{cv}) of various soft magnetic materials, and manufacturing cost of typical Fe-based nanocrystalline alloys. a) Relationship between the B_s and μ_e at 100 kHz of the typical soft magnetic materials. b) Relationship between the B_s and P_{cv} at 100 kHz and 0.2 T for soft magnetic materials. c) Schematics showing the dependence of μ_e at 100 kHz on the manufacturing cost of several typical Fe-based soft magnetic nanocrystalline compositions. The inset shows the FCMS ribbons with a width of 63 mm fabricated using industrial raw materials. d) Permeability values at high frequency of 100 kHz of various soft magnetic materials developed in different years.

present work, the μ_e of FCMS nanocrystalline alloy reaches an unprecedented 36 000 at 100 kHz, which is about 44% higher than that of FINEMET alloy. The advantage of permeability of FCMS is even larger at higher frequencies. Therefore, a combination of unprecedented high μ_e and extremely low P_{cv} at high frequencies, excellent annealing stability together with rattling manufacturing cost advantage and industrialization ability, have been achieved in the FCMS nanocrystalline alloy.

2.4. Origin of Excellent High-Frequency Soft Magnetic Properties

It is known that high μ_e of soft magnetic materials can be basically realized by reducing both average magnetocrystalline anisotropy ($<K_1>$) and magnetoelastic anisotropy (K_σ). According to the random anisotropy model, when the grain size is much smaller than the ferromagnetic exchange length (about 35 nm for Fe–Si based alloys),[15] the $<K_1>$ of alloy will be averaged and reduced, which is usually positively correlated with the grain size. Here, the average grain size of FCMS after optimal thermal treatment is only 11.8 nm which is smaller than the typical value of FeSiBCuNb

(about 13–15 nm), leading to a lower and neglectable $<K_1>$. Another important factor of K_σ is proportional to the saturation magnetostriction (λ_s) of the alloy.[47] The magnetostriction–field curve (λ–H) was measured using a magnetic strain method (Experimental Section). A standard sample of polycrystalline Ni ($\lambda_s = 33$ ppm) was first measured for calibration, and then the magnetostriction coefficients of FCMS and FeSiBCuNb alloy along the ribbon direction were measured. The variations of magnetostriction coefficient with the applied magnetic field were shown in Figure S12 (Supporting Information). We can see that the λ_s of both FCMS and commercial FeSiBCuNb nanocrystalline alloy was near zero. From the enlarged view, it can be seen that the λ_s of FCMS is slightly negative (about −1.5 ppm). The negative close-to-zero of λ_s of FCMS can also be attributed to the high density of ultrafine nanocrystals with an average size down to 11.8 nm, since the smaller grains and higher grain boundary density of FCMS lead to a larger volume fraction of 71.2%. The λ_s of FCMS can be simply estimated as the weighted average of the amorphous matrix and α-Fe nanocrystalline phases. As reported before, the λ_s of amorphous matrix is in the order of several tens' ppm, while the precipitated α-Fe phase is about -3 ppm for Fe–Si

**ADVANCED
SCIENCE NEWS**

www.advancedsciencenews.com

**ADVANCED
MATERIALS**

www.advmat.de

based alloys.[15] Therefore, it is reasonable that the FCMS with finer and denser nanocrystalline structures exhibits a close-to-zero and slightly negative λ_s, further leading to a close-to-zero K_σ of FCMS. The simultaneous proximity of $<K_1>$ and K_σ to zero contributes to the ultrahigh permeability of FCMS, which is related to the precipitation of nanoparticles with the smaller size. Noted that the absolute value of λ_s of FCMS is indeed slightly larger than that of commercial FeSiBCuNb nanocrystalline alloy. As a result, the overall magnetic anisotropy of FCMS is also slightly greater than that of commercial FeSiBCuNb nanocrystalline alloy, resulting in relatively low μ_e of FCMS at the frequency around 1 kHz as compared to that of commercial FeSiBCuNb nanocrystalline alloy. This is consistent with the results shown in Figure S11 (Supporting Information).

When operating at higher frequencies (above 30 kHz), the core loss and domain-wall motion mechanisms should become the crucial factors affecting the μ_e. At high frequencies, the large P_{cv} usually causes the deterioration of μ_e in soft magnetic materials.[48] It is known that the P_{cv} can be separated into three components: hysteresis loss, eddy current loss (P_e), and excess loss.[49] The hysteresis loss is very small when operating at high frequencies for soft magnetic materials with low H_c. The P_e can be described by[15] $P_e \propto d^2 f^2 B^2 / \rho_e$ (d is the ribbon thickness, f is the switching frequency, B is the magnetic induction amplitude, and ρ_e is the electrical resistivity). When d, f, and B are constant, P_e is inversely proportional to ρ_e. We measured the ρ_e of FCMS and commercial FeSiBCuNb nanocrystalline alloy by a standard four-probe method. As a result, the ρ_e of FCMS is close to that of commercial FeSiBCuNb nanocrystalline alloy, approximately 81 ± 2 $\mu\Omega$ cm. Therefore, the P_e of FCMS and commercial FeSiBCuNb nanocrystalline alloys should be at the same level. In addition, the excess loss originated from micro-eddy-currents surrounding the moving domain walls is also important to the final high-frequency total loss. Since high domain wall density will reduce excess losses by the decreasing of wall velocity, it is necessary to reduce the domain wall spacing for an amorphous ribbon material operating at high frequencies.[50,51] We observe the stroboscopic domain images at high frequencies up to 500 Hz for the optimal annealed FCMS (see Figure S13, Supporting Information) through a magneto-optical Kerr microscope. One can see from these figure that domain width becomes refined with the increasing frequency, which is commonly seen in soft magnetic materials.[50] None of them shows small patchy domains, indicating that the residual anisotropy was eliminated. The average width of domains in FCMS is around 18.5 μm at 500 Hz, which is slightly smaller than that of conventional nanocrystalline alloys.[52] Here, FCMS shows the smaller width of domains, resulting in the smaller excess loss,[53] thereby achieving efficient operation at high frequencies.

In addition to the static magnetic domain structures, FCMS also exhibits a unique response mechanism of magnetic domains under alternating magnetic field, which should have the decisive effect on its soft magnetic properties at high frequencies.[52] **Figure 5** shows the subset Kerr images for the dynamic evolution of the magnetic domain structures of FS and FCMS samples with the magnetic field swept parallel to the ribbon axis. As shown in the figure, the domain-wall motion mechanisms are quite different for FS and FCMS, resulting in a large difference in the high-frequency permeability for the two alloys. According to

the minimum energy principle,[54] when a magnetic field paralleled to the ribbon axis acts on a domain, the magnetic moments of the domains will eventually change along the magnetic-field direction. This process can occur through several mechanisms, i.e., reversible domain wall movements, irreversible domain wall movements, and spin rotation.[55] These domain-motion mechanisms exhibit distinct time constants which are responsible for the dynamics of the overall magnetization process, the so-called relaxation time. As the frequency of alternating magnetic field increasing, the domain motion mechanism with the longer relaxation time is unable to follow the field variation. Therefore, every deactivation of a domain motion mechanisms is always accompanied by the declination in μ_e at high frequencies. In the process of saturation, we observed that the domain walls of the FS mainly move in the plane of the ribbon, which is along the right-to-left direction (Figure 5a1–a6 and Video S1, Supporting Information). When an external magnetic field is applied, the domain walls first form at the location where the direction of magnetization closest to the direction of the external magnetic field. Then, with an increase in the intensity of the external field, the domain walls gradually expand from one side to the other side roughly along the direction of the magnetic field. The opposite magnetic moment near the domain wall rotates to the direction of the magnetic field, and the magnetic moment in the domain wall close to the direction of the magnetic field further rotates, gradually leaving the transition layer of the domain wall into another magnetic domain. Such domain wall movement mechanism in FS (Figure 5c) is common for soft magnetic ribbons or films.[56]

In sharp contrast, FCMS exhibits a domain-motion mechanism which is dominated by the spin rotation of domains from out and in plane (Figure 5b1–6 and Video S2, Supporting Information). From the magneto-optical Kerr images, one can see that there are many straight and narrow domains divided by domain walls, and they barely move upon the change of external magnetic field. The domain wall disappears instantaneously at a critical intensity when all the magnetic moments retroflex to the same direction from out of plane (the domain walls to be disappeared are marked by red arrows and those remaining are marked by black arrows in Figure 5b1–6). The spin rotation of domains results in the merging of adjacent domains (Figure 5d). No preferential rotation of spins occurs near the domain walls, but there is a critical "energy barrier" beyond which all the spins in the domain rotate simultaneously. Since the exclusion of the energy needed to overcome for domain wall movement, spin rotation has the lowest relaxation time. Therefore, the dominant mechanism of spin rotation in FCMS makes it easier to exhibit a strong magnetization at high frequencies, which is crucial for the higher high-frequency permeability. The distinguish magnetization mechanisms between FS and FCMS are caused by numerical differences in the saturation magnetostriction coefficient and the grain distribution. The large volume fraction of α-Fe in the amorphous matrix of FCMS greatly reduces the magnetostriction coefficient, resulting in the low K_σ, which is conducive to spin rotation. We emphasize that this spin-rotation dominated mechanism is totally different from that of FS and is rarely observed in previous studies of soft magnetic materials. This unique mechanism underpins the ultrahigh permeability of FCMS nanocrystalline alloy. The mechanism should be related to
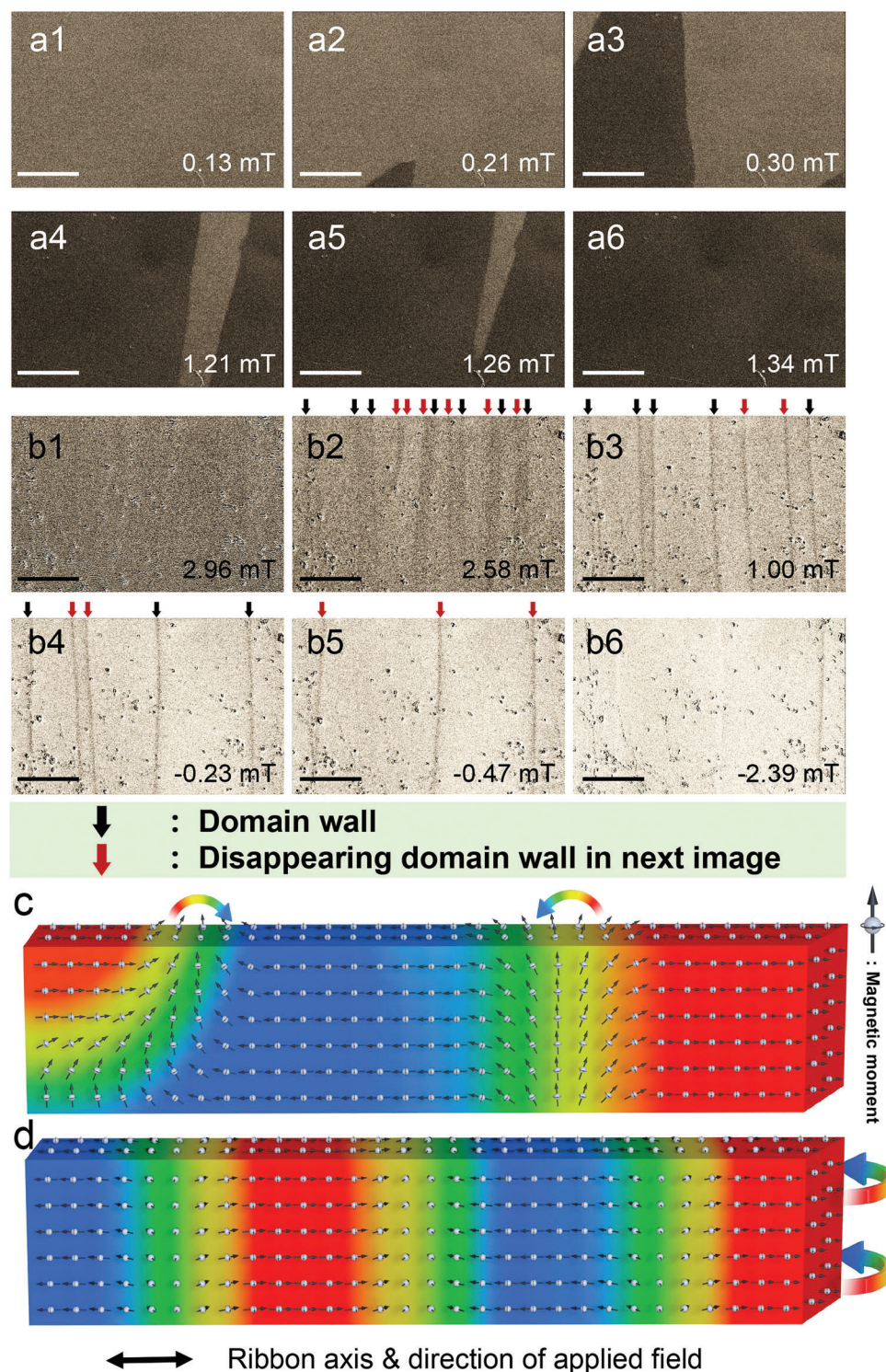
ADVANCED
SCIENCE NEWS

www.advancedsciencenews.com

ADVANCED
MATERIALS

www.advmat.de

Figure 5. Evolution of the magnetic domain structures of the FS and FCMS ribbons. a1–a6) Evolution of domain structure with different magnitudes of external magnetic fields of the FS ribbons sample using magneto-optical Kerr microscopy. b1–b6) Evolution of domain structure with different magnitudes of external magnetic fields of the FCMS ribbons sample using magneto-optical Kerr microscopy. The magnetic domains are indicated by the arrows at the top of the picture, thereinto, the domain walls pointed by red arrow disappear in the next domain image. The corresponding normalized magnetic field intensities are shown in each image. c) The schematic drawing of the domain wall movement mechanism on the surface of alloy ribbons from front view, where the arrows represent the motion of the in-plane magnetic moment when magnetized. d) The schematic drawing of the spin rotation mechanism on the surface of alloy ribbons from front view, where the arrows represent the motion of the out-of-plane magnetic moment when magnetized. The black double arrows indicate the ribbon axis and the direction of applied field.

the high grain-boundary density owing to the grain refinement in FCMS nanocrystalline alloy, which can effectively inhibit the movement of domain walls.

3. Conclusions

We have designed an ultrafine nanocrystalline–amorphous dual-phase structure in Fe-based amorphous alloys by microalloying of Co and Mo. Arising from the unique structure, the resultant $Fe_{75.5}Co_{0.5}Mo_{0.5}Cu_1Nb_{1.5}Si_{13}B_8$ alloy exhibits a combination of unprecedented high μ_e of 36 000 (maximum value) at 100 kHz (44% higher than that of commercial FeSiBCuNb nanocrystalline alloy), high B_s of 1.42 T (15% higher than that of commercial FeSiBCuNb nanocrystalline alloy), low P_{cv} of 120 kW m^{-3} at 0.2 T and 100 kHz, closing to that of commercial FeSiBCuNb nanocrystalline alloy. In addition, the alloy can also be fabricated into industrial wide ribbons with a manufacturability cost of 20% lower than that of commercial FeSiBCuNb nanocrystalline alloy. The superior properties of the $Fe_{75.5}Co_{0.5}Mo_{0.5}Cu_1Nb_{1.5}Si_{13}B_8$ alloy enables it as an ideal substitute to the traditional soft magnetic materials at high frequencies. The formation of this unique nanocrystalline–amorphous dual-phase structure can be attributed to a unique magnetic-heterogeneous nanocrystallization mechanism by microalloying Co and Mo, which is much different from that of the traditional nanocrystallization strategies by microalloying Cu and Nb. The present nanocrystallization mechanisms and the resultant nanocrystalline–amorphous dual-phase alloys provide a paradigm for the design of next-generation soft magnetic materials for wide energy-saving application prospects. In addition, the alloying strategy to induce the unique nanocrystallization and domain-motion mechanisms is also useful to discover more soft magnetic alloys with a series of superior properties.

4. Experimental Section

Materials Fabrication: Alloy ingots with nominal compositions of $Fe_{76.5}Cu_1Nb_{1.5}Si_{13}B_8$ (FS), $Fe_{76}Cu_1Nb_2Si_{13}B_8$ (FS′), $Fe_{76}Co_{0.5}Cu_1Nb_{1.5}Si_{13}B_8$ (FCS), $Fe_{76}Mo_{0.5}Cu_1Nb_{1.5}Si_{13}B_8$ (FMS), and $Fe_{75.5}Co_{0.5}Mo_{0.5}Cu_1Nb_{1.5}Si_{13}B_8$ (FCMS) were prepared by arc-melting a mixture of constituent elements with a purity of above 99.9 wt%. under an argon atmosphere. Each ingot was flipped over and remelted at least four times in order to obtain chemical homogeneity. Precursor amorphous ribbons with a thickness of 21 μm and a width of about 1 mm were fabricated in an argon atmosphere after high vacuum of about 1×10^{-3} Pa by the single roller melt-spinning method. The ingots of FCMS with weight of 500 kg were subsequently prepared by melting industrial grade raw materials of Fe (99 wt%), Si (99.85 wt%), Cu (99.95 wt%), Co (99.5 wt%), pre-alloy of Fe–B (18 wt%), Fe–Mo (50 wt%), and Fe–Nb (65 wt%) in air with an induction melting furnace, followed by an industrial grade single roller ribbon quenching device to produce ribbons with a width of 63 mm and a thickness of 17–18 μm. For comparison, the commercial FeSiBCuNb nanocrystalline ribbons with thickness of 17–18 μm were made from Advanced Technology and Materials Co., Ltd.

For subsequent annealing and dynamic magnetic properties test, the ribbons were cut and wound into a $30 \times 20 \times 10$ mm circular cores. Isothermal transverse magnetic annealing of the as-quenched ribbons and cores was carried out in a high-purity argon flow and in flowing nitrogen atmosphere, respectively, at the temperature of 853 K and various time ranges from 10 to 30 min. Magnetic field annealing was applied with an in-plane magnetic field perpendicular to the ribbon direction in the entire process with a magnetic field of 0.1 T.

Structure Characterization: A Bruker D8 ADVANCE XRD and a Netzsch 404 F3 DSC which were performed at a constant heating rate of 20 K min^{-1} were utilized to confirm the amorphous features and research the isothermal behaviors of these alloys. Microstructures and atomic element distributions of the as-quenched and annealed samples were characterized by a JEM F200 TEM with a field-emission gun operated at 300 kV and a CAMEACA LEAP 5000 XR 3D-APT. Needle-shaped specimens required for 3D-APT were fabricated by lift-outs and annular milled in a FEI Scios focused ion beam/scanning electron microscope (FIB/SEM). The specimens were analyzed at 70 K in voltage mode, at a pulse repetition rate of 200 kHz, a pulse fraction of 20%, and an evaporation detection rate of 0.2% atom per pulse. Imago Visualization and Analysis Software (IVAS) version 3.8 was used for creating the 3D reconstructions and data analysis. The SAXS experiments were performed at beamline 12-ID-B at APS, ANL with X-ray energy of 13.3 keV. The exposure time was set to 2 s for each pattern. The 2D scattering images were collected continuously by a Pilatus 2 M detector. The data were integrated by a built-in code in Matlab first and then analyzed using the Irena package.[57] The fitted radius of gyration, R_g, quantifies the average size of the scatters, namely the crystalline nuclei radius, which is obtained by Guinier-porod fitting on SAXS data.[24]

The crystallization volume fraction of all samples using the method by analyzing the bright-field TEM images.[58,59] First, the number density (N_d) of α-Fe (Si) grains was estimated by $N_d = N/(A \times D)$, where N is quantity of the crystals and clusters appeared in TEM image, and A is the area of the TEM image. The V_{cry} was then estimated by using the equation $V_{cry} = N_d\pi D^3/6$, where D is the average size of α-Fe (Si) grains. The grain boundary density is evaluated by the following equation: $\rho_g = (A_g/V_g) \times V_{cry}$, where A_g is the average grain surface area, V_g is the average grain volume. Assuming that the precipitated α-Fe (Si) grain has an ideal spherical shape, A_g can be calculated by: $A_g = 4\pi(D/2)^2$, and V_g can be calculated by: $V_g = (4\pi/3)(D/2)^3$, where D is the average size of α-Fe (Si) grains.

Magnetic Property Measurements: The ribbons were wound into circular cores of the same size (outer diameter × inner diameter × height: $30 \times 20 \times 10$ mm) for the characterization of magnetic properties, eliminating the measurement error caused by the shape and magnetic leakage effect. The thickness of FCMS and commercial FeSiBCuNb nanocrystalline alloys were 17–18 μm. Magnetic properties including B_s, H_c, μ_e and iron loss were measured with a Quantum Design MPMS3 vibrating sample magnetometer under the maximum applied field of 400 Oe, a EXPH 100 B–H loop tracer under a field of 800 A m^{-1}, an Agilent 4294A impedance analyzer under the applied field of 1 A m^{-1} and a BH-100k AC B–H loop tracer, respectively. After recording the inductance values using an impedance analyzer, the data were converted by the following formula to obtain the effective permeability of the material at frequencies from 1 kHz to 1 MHz.

$$L = \frac{\mu_e N^2 A_e}{L_e} \tag{1}$$

where L is the inductance, μ_e is the effective permeability, N is the number of coil turns (1 turn), A_e is the effective cross-sectional area, L_e is the effective magnetic circuit length (A_e and L_e can be converted by core size and lamination coefficient). The total loss of FCMS and commercial FeSiBCuNb nanocrystalline alloy cores were tested on an AC B–H loop tracer (SY-8258). The electrical resistivity of alloys was measured by the four-wire method using Physical Property Measurement System (Quantum Design DynaCool).

The magnetostriction–field curve (λ–H) was measured in a home-made pulsed magnetic field. The pulsed magnetic field is produced by a pulse magnet which consists of a bank of charged capacitors and a drive coil with length × diameter ($L \times D$) = 100×100 mm^2. The pulsed magnet can generate damping sine-wave magnetic fields with peak strength of ±16 T with time constant of 12 ms. The test equipment includes a strain gauge as strain sensor in an ac bridge, a Stanford Research Systems lock-in amplifier

(SR865A) for strain signal conditioning, an oscilloscope (ZLG ZHIYUAN Electronics, ZDS3024) for data acquiring and recording, and a personal computer for data processing. The resolution of the magnetostriction coefficient measurement set-up is 2 ppm.

Magnetic domains and magnetic domain motion upon the external magnetic field were observed by an em-Kerr-highres magneto-optical Kerr microscope. Three specimens have been tested for each measurement to ensure the repeatability, and all the measurements were performed at room temperature. The width of magnetic domain was evaluated by the average value of each width of visible magnetic domains in magneto-optical Kerr images.

Molecular-Dynamics Simulation Method: Classical molecular-dynamics simulations were conducted on Fe–Co alloys using spin-lattice dynamics model to account for the coupling between the spin and mechanical relaxations,[60,61] with the Hamiltonian of the system written as:

$$H\left(\vec{r}, \vec{p}, \vec{s}\right) = H_{\mathrm{mag}}\left(\vec{r}, \vec{s}\right) + \sum_{i=1}^{N} \frac{\vec{p}_i}{2m_i} + \sum_{i,j=1}^{N} U\left(\vec{r}_{ij}\right) \tag{2}$$

where $\vec{r}_i$, $\vec{p}_i$, $\vec{s}_i$ and $\vec{m}_i$ designate the position, momentum, normalized magnetic moment and mass of atom i, respectively. $U(\vec{r}_{ij})$ is the interatomic potential energy, formulated by the embedded-atom method (EAM) with the force-field parameter adjusted for Fe–Co alloys.[62] $H_{\mathrm{mag}}(\vec{r}, \vec{s})$ is the interatomic magnetic energy:

$$H_{\mathrm{mag}}\left(\vec{r}, \vec{s}\right) = -g \sum_{i=1}^{N} \mu_i \vec{s}_i \cdot \vec{H}_{\mathrm{ext}} - \sum_{i \neq j}^{N} J\left(r_{ij}\right) \vec{s}_i \cdot \vec{s}_j + H_{\mathrm{N\acute{e}el}}\left(\vec{r}, \vec{s}\right) \tag{3}$$

where g is the Landé factor, μ_i is the atomic moment given as a multiple of the Bohr magneton, and $\vec{H}_{\mathrm{ext}}$ is the external magnetic field. $J(r_{ij})$ is the Heisenberg magnetic coupling exchange parameter. $H_{\mathrm{N\acute{e}el}}(\vec{r}, \vec{s})$ is the Néel term describing interaction between pairs of magnetic spins:

$$H_{\mathrm{N\acute{e}el}}\left(\vec{r}, \vec{s}\right) = -\sum_{i \neq j}^{N} g_1\left(r_{ij}\right) \left(\left(\vec{e}_{ij} \cdot \vec{s}_i\right) \left(\vec{e}_{ij} \cdot \vec{s}_j\right) - \frac{\vec{s}_i \cdot \vec{s}_j}{3} \right) \tag{4}$$

where $\vec{e}_{ij} = \vec{r}_{ij} / r_{ij}$. The term $g_1(r_{ij})$ describes the dipole interaction, and can be written in form of the Bethe–Slater function as the exchange term $J(r_{ij})$:

$$J\left(r_{ij}\right) = 4a \left(\frac{r_{ij}}{d}\right)^2 \left(1 - b \left(\frac{r_{ij}}{d}\right)^2\right) e^{-\left(\frac{r_{ij}}{d}\right)^2} \Theta\left(R_c - r_{ij}\right) \tag{5}$$

where a, b, and d are the constant coefficients needed to be fitted to the exchange interaction for $J(r_{ij})$, and to the magnetoelastic interaction for $g_1(r_{ij})$. Θ is the Heaviside step function with R_c (the cutoff radius). These interactions have been implemented in the SPIN package[61] of LAMMPS,[63] based on which the simulations were performed in this work. These magnetic force-field parameters are taken from ref. [64] for Fe element, and from ref. [65] for Co element. The cross-interaction parameters between Fe and Co atoms adopt the value averaging over Fe and Co for a, b, and d. The mechanical forces have been offset by the exchange interaction to counter the implicitly comprised magnetic interaction in the EAM potential.

The simulations started at 2000 K for $Fe_{95}Co_5$ melts with atoms randomly placed in a cubic box containing 5000 atoms. After a short-time relaxation, the melts were quenched to 750 K in a cooling rate about 10^{13} K s^{-1}, with the simulation timestep set as 1 fs. Glass transition temperature was determined at about 900 K from the volume evolution in the alloys during the cooling process (Figure S14a, Supporting Information). Curie temperature, T_C, is measured at about 1000 K for the $Fe_{95}Co_5$ metallic glasses, close to the experimentally measured T_C (1040 K) in α-Fe (Figure S14b, Supporting Information). The alloys were relaxed at 750 K at the presence of different external magnetic fields, i.e., $H_{\mathrm{ext}} = 0$ and 1 T. A long-time relaxation was performed until the melt crystallized. The incubation time is defined as the waiting time for the crystallization happening. Twenty ensembles with different random seeds for the initial configurations were used to calculate the average incubation time. Bond orientational order parameter[66,67] was utilized to identify the atoms of crystal-like order during the crystallization process.

Supporting Information

Supporting Information is available from the Wiley Online Library or from the author.

Conflict of Interest

The authors declare no conflict of interest.

Author Contributions

H.Y.B., B.A.S., and W.H.W. conceived and supervised the project. J.Z. and X.S.L. prepared materials and performed the XRD, DSC, and TEM experiments. X.D.F., X.B.H., and J.G.W. performed magnetic tests. J.H.L. and C.T.L. preformed the 3D-APT tests. H.L.P. performed simulation analysis. Q.S.Z. and H.B.L. performed the SAXS measurement. H.Y.B., B.A.S., X.S.L., and J.Z. performed data analysis and wrote the manuscript with the input of all other co-authors. W.H.W., B.L.S., and H.B.K. discussed the results and commented on the manuscript.

Data Availability Statement

The data that support the findings of this study are available from the corresponding author upon reasonable request.

ADVANCED
SCIENCE NEWS

www.advancedsciencenews.com

ADVANCED
MATERIALS

www.advmat.de

[1] J. Silveyra, E. Ferrara, D. L. Huber, T. C. Monson, *Science* **2018**, *362*, eaao0195.

[2] M. Niethammer, M. Widmann, T. Rendler, N. Morioka, Y. C. Chen, R. Stohr, J. Hassan, S. Onoda, T. Ohshima, S. Y. Lee, A. Mukherjee, J. Isoya, N. T. Son, J. Wrachtrup, *Nat. Commun.* **2019**, *10*, 5569.

[3] X. H. Li, L. Lou, W. P. Song, G. W. Huang, F. C. Hou, Q. Zhang, H. T. Zhang, J. W. Xiao, B. Wen, X. Y. Zhang, *Adv. Mater.* **2017**, *29*, 1606430.

[4] O. Gutfleisch, M. A. Willard, E. Brück, C. H. Chen, S. G. Sankar, J. P. Liu, *Adv. Mater.* **2011**, *23*, 821.

[5] W. J. Liu, H. X. Zhang, J. A. Shi, Z. C. Wang, C. Song, X. R. Wang, S. Y. Lu, X. J. Zhou, L. Gu, D. V. Louzguine-Luzgin, M. W. Chen, K. F. Yao, N. Chen, *Nat. Commun.* **2016**, *7*, 13497.

[6] F. Fiorillo, G. Bertotti, C. Appino, M. Pasquale, in *Wiley Encyclopedia of Electrical and Electronics Engineering*, John Wiley & Sons, Inc., Weinheim, Germany **2016**, pp. 1–42.

[7] M. Nakamura, O. Ishii, S. Horikoshi, S. Kambe, *IEEE Trans. Magn.* **2004**, *40*, 2733.

[8] J. A. Ewing, *Magnetic Induction in Iron and Other Metals*, The Electrician Printing and Publishing Co. Limited, London, UK 1900.

[9] M. de Vries, 80 Years of Research at the Philips Natuurkundig Laboratorium (1914-1994). The Role of the Nat. Lab. at Philips, Amsterdam University Press, Amsterdam, The Netherlands **2005**.

[10] Y. Yoshizawa, S. Oguma, K. Yamauchi, *J. Appl. Phys.* **1988**, *64*, 6044.

[11] P. Duwez, S. C. H. Lin, *J. Appl. Phys.* **1967**, *38*, 4096.

[12] H. Li, A. D. Wang, T. Liu, P. B. Chen, A. N. He, Q. Li, J. H. Luan, C. T. Liu, *Mater. Today* **2021**, *42*, 49.

[13] H. Y. Xiao, Y. Q. Dong, A. N. He, H. Sun, A. D. Wang, H. Li, L. Liu, X. C. Liu, R. W. Li, *J. Magn. Magn. Mater.* **2019**, *478*, 192.

[14] X. S. Li, J. Zhou, L. Q. Shen, B. A. Sun, H. Y. Bai, W. H. Wang, *Adv. Mater.* **2022**, *2205863*

[15] M. A. Willard, *Handbook of Magnetic Materials*, Vol. *21*, Elsevier, Oxford, UK **2013**, p. 173.

[16] M. F. Jiang, M. J. Cai, J. Zhou, S. Y. Di, X. S. Li, Q. Luo, B. L. Shen, *Mater. Today Nano* **2023**, *22*, 100307.

[17] M. E. McHenry, M. A. Willard, D. E. Laughlin, *Prog. Mater. Sci.* **1999**, *44*, 291.

[18] G. Herzer, *Acta Mater.* **2013**, *61*, 718.

[19] Y. J. Xie, S. Sohn, M. L. Wang, H. L. Xin, Y. Jung, M. D. Shattuck, C. S. O'Hern, J. Schroers, J. J. Cha, *Nat. Commun.* **2019**, *10*, 915.

[20] Y. M. Chen, T. Ohkubo, Y. Yoshizawa, K. Hono, *Acta Mater.* **2009**, *57*, 4463.

[21] K. Hono, D. H. Ping, M. Ohnuma, H. Onodera, *Acta Mater.* **1999**, *3*, 997.

[22] Y. Q. Cheng, E. Ma, *Prog. Mater. Sci.* **2011**, *56*, 379.

[23] A. Takeuchi, A. Inoue, *Mater. Trans.* **2005**, *46*, 2817.

[24] H. B. Lou, Z. D. Zeng, F. Zhang, S. Y. Chen, P. Luo, X. H. Chen, Y. Ren, V. B. Prakapenka, C. Prescher, X. B. Zou, T. Li, J. G. Wen, W. H. Wang, H. W. Sheng, Q. S. Zeng, *Nat. Commun.* **2020**, *11*, 314.

[25] C. L. Zhao, A. D. Wang, A. N. He, C. T. Chang, C. T. Liu, *Sci. China Mater.* **2021**, *64*, 1813.

[26] G. Herzer, *IEEE Trans. Magn.* **2002**, *26*, 1397.

[27] L. X. Shi, K. F. Yao, *Mater. Des.* **2020**, *189*, 108511.

[28] Y. Yoshizawa, S. Fujii, D. H. Ping, M. Ohnuma, K. Hono, *Mater. Sci. Eng., A* **2004**, *375*, 207.

[29] R. Parsons, B. Zhang, K. Onodera, H. Kishimoto, A. Kato, K. Suzuki, *J. Alloys Compd.* **2007**, *723*, 408.

[30] J. Y. Park, K. Y. Kim, T. H. Noh, S. J. Suh, *Mater. Sci. Eng., A* **1997**, *226*, 685.

[31] S. Kwon, S. Kim, H. Yim, K. H. Hang, C. S. Yoon, *J. Alloys Compd.* **2020**, *826*, 154136.

[32] F. P. Wan, T. Liu, F. Y. Kong, A. D. Wang, M. Q. Tian, J. C. Song, J. H. Zhang, C. T. Chang, X. M. Wang, *Mater. Res. Bull.* **2017**, *96*, 275.

[33] Y. Yoshizawa, S. Fujii, D. H. Ping, M. Ohnuma, K. Hono, *Scr. Mater.* **2003**, *48*, 863.

[34] T. Liu, F. Y. Kong, L. Xie, A. D. Wang, C. T. Chang, X. M. Wang, C. T. Liu, *J. Magn. Magn. Mater.* **2017**, *441*, 174.

[35] J. Zhou, W. M. Yang, C. C. Yuan, B. A. Sun, B. L. Shen, *J. Alloys Compd.* **2018**, *742*, 318.

[36] W. M. Yang, H. S. Liu, Y. C. Zhao, A. Inoue, K. M. Jiang, J. T. Hou, H. B. Ling, Q. Li, B. L. Shen, *Sci. Rep.* **2014**, *4*, 6233.

[37] J. Zhou, Q. Q. Wang, X. D. Hui, Q. S. Zeng, Y. W. Xiong, K. B. Yin, B. A. Sun, L. T. Sun, M. H. Stojca, W. H. Wang, B. L. Shen, *Mater. Des.* **2020**, *191*, 108597.

[38] A. D. Wang, M. X. Zhang, J. H. Zhang, H. Men, B. L. Shen, S. J. Pang, T. Zhang, *J. Alloys Compd.* **2012**, *536*, S354.

[39] J. Zhou, B. A. Sun, Q. Q. Wang, Q. M. Yang, W. M. Yang, B. L. Shen, *J. Alloys Compd.* **2019**, *783*, 555.

[40] K. Q. Jiang, K. Li, C. Peng, Y. Zhu, *J. Alloys Compd.* **2012**, *541*, 472.

[41] V. Tsakaloudi, G. Kogias, V. T. Zaspalis, *J. Alloys Compd.* **2014**, *588*, 222.

[42] Z. H. Khan, M. Mahbubur Rahman, S. S. Hakim, D. K. Saha, *J. Alloys Compd.* **2013**, *548*, 208.

[43] T. Nakamura, T. Miyamoto, Y. Yamada, *J. Magn. Magn. Mater.* **2003**, *256*, 340.

[44] T. Tsutaoka, *J. Appl. Phys.* **2003**, *93*, 2789.

[45] J. H. Yang, Y. B. Kim, K. S. Ryu, M. J. Kim, Y. C. Chung, T. K. Kim, *J. Magn. Magn. Mater.* **2000**, *222*, 65.

[46] Y. Cao, F. Y. Yang, J. W. Li, A. N. He, A. D. Wang, H. Y. Xiao, Y. Q. Dong, X. C. Liu, B. J. Zhang, Y. Han, *J. Magn. Magn. Mater.* **2021**, *526*, 167691.

[47] G. Herzer, *J. Magn. Magn. Mater.* **1992**, *112*, 258.

[48] C. S. Tsai, W. J. Yang, M. S. Leu, C. S. Lin, *J. Appl. Phys.* **1991**, *70*, 5846.

[49] G. Bertotti, *Hysteresis in Magnetism: For Physicists, Materials Scientists, and Engineers*, Academic Press, San Diego, CA, USA **1998**.

[50] S. Flohrer, R. Schafer, J. McCord, S. Roth, L. Schultz, F. Fiorillo, W. Gunther, G. Herzer, *Acta Mater.* **2006**, *54*, 4693.

[51] R. H. Zhang, A. N. He, L. Xie, J. H. Zhang, Y. Q. Dong, J. W. Li, B. J. Zhang, Y. X. Liu, *J. Alloys Compd.* **2021**, *891*, 161956.

[52] E. Ferrara, C. De Luigi, C. Beatrice, C. Appino, F. Fiorllo, *J. Magn. Magn. Mater.* **2000**, *215*, 466.

[53] G. Bertotti, *IEEE Trans. Magn.* **1988**, *24*, 621.

[54] J. S. Kim, M. A. Mawass, A. Bisig, B. Kruger, R. M. Reeve, T. Schulz, F. Buttner, J. Yoon, C. Y. You, M. Weigand, H. Stoll, G. Schutz, H. J. M. Swagten, B. Koopmans, S. Eisebitt, M. Klaui, *Nat. Commun.* **2014**, *5*, 3429.

[55] E. A. Perigo, B. Weidenfeller, P. Kollar, J. Fuzee, *Appl. Phys. Rev.* **2018**, *5*, 031301.

[56] F. Magnus, R. Moubah, U. B. Arnalds, V. Kapaklis, A. Brunner, R. Schafer, G. Andersson, B. Hjorvarsson, *Phys. Rev. B* **2014**, *89*, 224420.

[57] J. Ilavsky, P. R. Jemian, *J. Appl. Crystallogr.* **2009**, *42*, 347.

[58] X. J. Jia, W. Zhang, Y. Q. Dong, J. W. Li, A. N. He, J. H. Luan, R. W. Li, *J. Alloys Compd.* **2022**, *920*, 166030.

[59] X. J. Jia, Y. H. Li, L. C. Wu, Y. Zhang, L. Xie, W. Zhang, *J. Mater. Sci.* **2019**, *54*, 4400.

[60] P. W. Ma, S. L. Dudarev, C. H. Woo, *Comput. Phys. Commun.* **2016**, *207*, 350.

[61] J. Tranchida, S. L. Plimpton, P. Thibaudeau, A. P. Thompson, *J Comput Phys* **2018**, *372*, 406.

[62] H. Chamati, N. I. Papanicolaou, Y. Mishin, D. A. Papaconstantopoulos, *Surf. Sci.* **2006**, *600*, 1793.

[63] S. Plimpton, *J. Comput. Phys.* **1995**, *117*, 1.

[64] P. Nieves, J. Tranchida, S. Nikolov, A. Fraile, D. Legut, *Phys. Rev. B* **2022**, *105*, 134430.

[65] D. Beaujouan, P. Thibaudeau, C. Barreteau, *Phys. Rev. B* **2012**, *86*, 174409.

[66] P. J. Steinhardt, D. R. Nelson, M. Ronchetti, *Phys. Rev. B* **1983**, *28*, 784.

[67] M. Leocmach, H. Tanaka, *Nat. Commun.* **2012**, *3*, 974.